Desalination and Water Treatment
www.deswater.com

doi: 10.5004/dwt.2019.23545

144 (2019) 26–38
March

Influence of GRAFIM® content and the presence of silver nanoparticles on PSf composite membrane properties

Priscila Anadão*, Hélio Wiebeck

[a]*Engineering School, Metallurgical and Materials Engineering Department, University of São Paulo, Av. Prof. Mello Moraes, 2463, CEP 05508-900, Cidade Universitária, São Paulo, Brazil, Tel. (+5511) 3091-5236; emails: priscila.anadao@gmail.com (P. Anadão), hwiebeck@usp.br (H. Wiebeck)*

Received 14 March 2018; Accepted 28 November 2018

ABSTRACT

Rheology assessment is an important tool to understand membrane process formation as well as membrane morphology and properties. Hence, by varying the GRAFIM® content and adding silver nanoparticles, polysulfone composite membranes were prepared through the wet-phase inversion method with *N*-methyl-2-pyrrolidone as a solvent and water as a nonsolvent. Newtonian fluids were obtained, and silver nanoparticle dispersions presented the highest viscosities. Water diffusion was Fickian in both systems, and their coefficients decreased by increasing their viscosity. Dense surfaces characterized GRAFIM® membranes, whereas nanoporous surfaces were present in silver nanoparticle membranes due to their higher dispersion viscosity. Both thermodynamical favoring and rheological hindrance led to membrane formation. GRAFIM® and silver nanoparticles positively influenced water sorption, linear expansion, porosity, and hydrophilicity. Finally, these membranes presented high values of water permeability due to their high porosity, cutoff in the range of nanofiltration, which were lower for the membranes with only GRAFIM® and favorable values of saline rejection for four used salts (NaCl, Na_2SO_4, $MgCl_2$, and $MgSO_4$).

Keywords: Polysulfone; Composite membrane; GRAFIM®; Membrane formation; Membrane morphology; Nanofiltration

1. Introduction

The depletion of natural resources makes entities, which are responsible for providing drinking water for the population, invest in capturing and treating water. Due to increasing environmental pollution, certain water treatments, which have been used so far, no longer result in good quality and require high-performance industrial processes. Hence, many researches are aimed at technologies that present both efficient technical results and financial-economic viability to compete with the existing processes. Therefore, attention has been paid to membrane technology since it is a clean versatile type and able to remove contaminants from micrometer to nanometer scales [1–7].

The material generally chosen to prepare membranes is polymer because one of its advantages is its relative ease to produce a thin film, which allows the obtention of high permeability rates at a low cost. However, polymer membranes have several limitations, such as low selectivity, high temperature instability and dilatation, and decomposition in solvent. One of the most widely used polymers is polysulfone (PSf) for its low cost, availability, high mechanical strength, thermal and chemical stabilities, easy processability, and variety of active functional groups [8].

The most widely used method to produce polymer membrane is incorporating an additive in the phase-inversion process, thus overcoming possible disadvantages polymers can have. Besides the improvements provided by the composite or nanocomposite formation [9], other advantages are

* Corresponding author.

rheology improvement, increased lifetime, macrovoid suppression, and better connectivity between the pores. These improvements in membrane morphology directly reflect on the increase of membrane permeability and rejection [10]. Several types of additives have been used in membrane preparation, such as titania [11–13], zirconia [14,15], clay [16–18], zeolites [19–21], and allotrope forms of carbon [4,22–24].

In recent years, the addition of carbonous materials, such as carbon nanotubes [25–28], has demonstrated its potential to improve membrane properties and to control membrane morphology. Moreover, activated carbon modified PSf membrane morphology and increased membrane hydrophilicity [29]. We thus decided to understand the influence of a new graphene-based material called GRAFIM®.

GRAFIM® is formed by a mesoporous polyhedral nanostructure composed of graphene plans (Fig. 1). They are modelled and tipped during the production process to form regular cells and channels, which besides special electrical conductivity generates excellent absorption properties as GRAFIM® has a broad specific surface area. Besides these characteristics, due to its peculiar structure, GRAFIM® is a crystalline, inert, nonflammable, and completely stable material without any risk to human health or to the environment since nanofibers, nanotubes, and other nanoparticles are integrated in specific ways, being contained within the material cells. Because of this, interesting intermolecular interactions can be established between GRAFIM® and PSf chains to improve the final membrane properties. Moreover, by adding GRAFIM® particles, preferable paths of permeation can be created, originating a selective permeation by imposing a barrier to certain solutes and then improving the separation performance [30]. Some important data related to its surface area pore size and volume about GRAFIM® are presented in Table 1 and its morphology is depicted by a transmission electron microscopy (TEM) image in Fig. 2.

Table 1
GRAFIM® chemical information data

Property	Value
Brunauer–Emmett–Teller (BET) surface area	458.4048 $m^2 g^{-1}$
Langmuir surface area	620.1250 $m^2 g^{-1}$
Barrett-Joyner-Halenda (BJH) adsorption cumulative surface area of pores between 1.7000 and 300.0000 nm diameter	156.537 $m^2 g^{-1}$
BJH desorption cumulative surface area of pores between 1.7000 and 300.0000 nm diameter	171.8280 $m^2 g^{-1}$
Adsorption average pore width (4*V*/*A* by BET)	2.76200 nm
Desorption average pore width (4*V*/*A* by BET)	2.84041 nm
BJH adsorption average pore diameter (4*V*/*A*)	5.1622 nm
BJH desorption average pore diameter (4*V*/*A*)	4.8468 nm
Single-point adsorption total pore volume of pores less than 123.7106 nm diameter at *P*/Po = 0.984099916	0.316528 $cm^3 g^{-1}$
Single-point desorption total pore volume of pores less than 104.0815 nm diameter at *P*/Po = 0.981038649	0.325514 $cm^3 g^{-1}$
BJH adsorption cumulative volume of pores between 1.7000 and 300.0000 nm diameter	0.202019 $cm^3 g^{-1}$
BJH desorption cumulative volume of pores between 1.7000 and 300.0000 nm diameter	0.208206 $cm^3 g^{-1}$

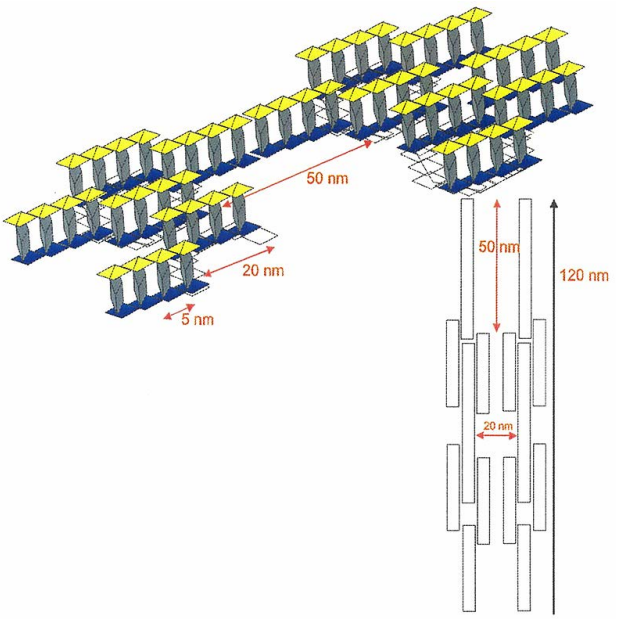

Fig. 1. Schematic representation of GRAFIM®.

Another additive generally employed in filtration membrane is silver nanoparticles. These nanoparticles are hydrophilic, increasing water permeability, and present antibacterial properties, helping to control biofouling formation [31–33]. Thus, this additive will also be incorporated in our study.

As different components are added to the ternary system composed of polymer/solvent/nonsolvent, it is interesting to understand the rheology of the resulting systems, once rheological properties play an important role in determining the membrane morphology. Casting dispersion viscosity is known to influence the exchange between solvent and nonsolvent and the kinetics during membrane preparation through the wet-phase inversion method [34–36]. Moreover, membrane properties, such as porosity and water sorption, are also a result of dispersion viscosity. Therefore, the main aim of this research is to present a study on the rheology of the systems PSf/NMP/GRAFIM® and PSf/NMP/GRAFIM®+silver nanoparticles (Ag) and to correlate these results with the deriving membranes prepared through the wet-phase inversion method by using water as a nonsolvent. The kinetics of both systems and membrane morphology and properties will be discussed in terms of viscosity.

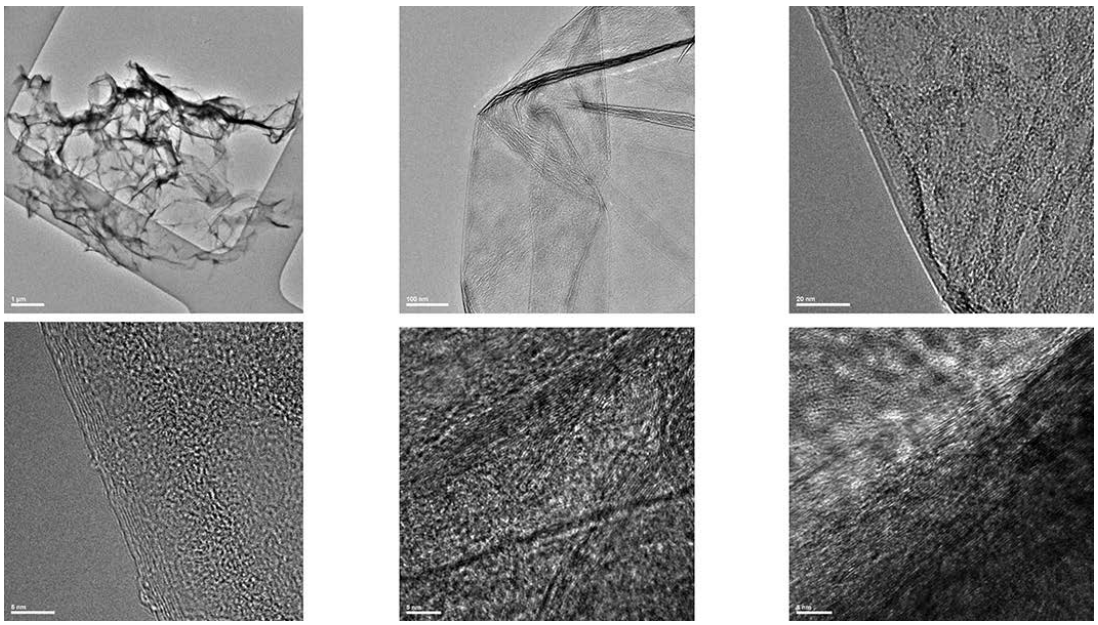

Fig. 2. GRAFIM® TEM image.

2. Materials and methods

2.1. Materials

PSf Udel® P-3500 was gently supplied by Solvay Advanced Polymers. *N*-methyl-2-pyrrolidone (NMP) was used as a solvent and distilled water as a nonsolvent. GRAFIM® was provided by GrapheneUP SE. Silver nanoparticles were also used.

2.2. Silver nanoparticle preparation

Silver nanoparticles were prepared through the alcohol-reduction method [37,38], from a silver nitrate solution, in the presence of polyvinylpyrrolidone (PVP) as a protecting agent. In this method, in a 500-mL reactor, 95 g of a solution containing 5 wt.% PVP, 5 g of ethanol, and 1.85M silver nitrate were added, under stirring and N_2 flux. This mixture was heated at 50°C under reflux for 30 min, which changed its color from slightly yellow to dark brown, and it was immediately cooled in an ice bath. Finally, the mixture was centrifuged at 15,000 rpm for 25 min. The transparent solution was discarded, and the pellets of silver nanoparticles were collected, being stored at −16°C.

These silver nanoparticles were characterized by a TEM and ultraviolet-visible spectroscopy (UV-Vis) spectroscopy. TEM measurements were performed from dilutions of the original dispersions by dripping an aliquot over a copper grid covered with carbon and formvar, drying slowly in a laminar flow and subsequently in vacuum for 4 h.

2.3. Dispersion preparation and characterization

The casting dispersions for the preparation of the membranes consisted of 25 wt.% PSf in NMP. Dispersions containing 0.5, 1.0, and 2.0 wt.% GRAFIM® were prepared in a high-speed mixer for 6 h to obtain a homogeneous particle dispersion. Two versions were prepared: one by adding a 1,000 ppm silver nanoparticle solution and the other without these nanoparticles. The viscosities of all dispersions were determined using a Brookfield Viscometer (Model DV-II + CP 52) in a constant shear experiment at 25°C. A shear stress, which is defined as a force applied to the interface mobile surface and dispersion, is imposed, and it causes a flux on the dispersion. The shear rate is the inverse of the flux of velocity that can be maintained by this force which is controlled by the internal liquid resistance. The samples were bubble free during the rheological measurements. The extrapolation of shear forces measured for a zero shear rate provided the absolute viscosity.

2.4. Membrane preparation

Each dispersion was spread as a viscous film onto a glass plate with a knife. After this, this glass plate was immediately immersed into a glass recipient which was the precipitation medium containing distilled water at 60°C; the temperature was rigorously controlled with a heating bath. The exchange between solvent and nonsolvent promoted membrane formation.

2.5. Coagulation time

The period from when polymer dispersion is immersed into the coagulation bath until demixing is finalized, which includes the time of diffusion of both solvent and nonsolvent across the interface between casting dispersion and coagulation bath, is defined as coagulation time. The moment demixing was concluded, the membrane became gray, opaque, and completely detached from the glass plate. Aiming to determine kinetic parameters, the coagulation time of each membrane was measured in triplicates by using a stopwatch and the wet membrane thickness was measured carefully by using

a Vernier caliper. This experiment was conducted at 60°C and rigorously controlled with a heating bath. The diffusion coefficient (D) was then calculated by using Eq. (1):

$$D = \frac{d^2}{t} \tag{1}$$

in which d^2 (cm^2) and t (s) represent the square of wet membrane thickness and the coagulation time, respectively [39].

2.6. Scanning electron microscopy

A scanning electron microscopy (SEM) FEI QUANTA 600 FEG was used to analyze the surfaces and the cross sections of the membranes. Samples were sputter-coated with platinum by a Bal-tec SCD 050 metaliser, and the cross sections were cryogenically fractured.

2.7. Atomic force microscopy

Atomic force microscopy is a powerful tool for the membrane characterization which allows the determination of surface morphology without any special sample preparation. Topographic maps were obtained by scanning with a silicon nitride probe over membrane surface, characterizing contact mode, in which the probe rapidly responds to the repulsive forces. The atomic force microscope used in this study was a Microscope Shimadzu SPM 9500J3, 30 μm scans with a 1 cm × 1 cm sample. An area of 5 μm × 5 μm was scanned at a rate of 1 Hz for each sample.

2.8. Porosity measurement

Each membrane maintained in distilled water, after having its surface water removed by a tissue, was weighed. Later, they were placed in an air-circulation oven at 60°C for 24 h and then dried in a vacuum oven at 80°C for 24 h, having their weights measured after these procedures, as described elsewhere [39]. Hence, considering both weights, porosity was calculated using Eq. (2):

$$P(\%) = \frac{(Q_0 - Q_1)}{A \times h} \times 1{,}000 \tag{2}$$

in which P is the membrane porosity, Q_0 is the wet sample weight (g), Q_1 is the dry sample weight (g), A is the square of the membrane (cm^2), and h its thickness (mm). Five samples were considered to obtain an average value.

2.9. Water sorption and linear expansion

Each wet membrane, with 4 cm^2 × 4 cm^2, had its external water removed with a tissue; its weight was measured on an analytical scale, and its length was measured with a caliper. After this, the sample was dried in a vacuum oven at 100°C for 3 h, and both parameters were measured again. The linear expansion (L%) [Eq. (3)] and the water sorption (W%) [Eq. (4)] were then calculated:

$$L\% = \frac{(L_1 - L_0)}{L_0} \times 100 \tag{3}$$

$$W\% = \frac{W_1 - W_0}{W_0} \times 100 \tag{4}$$

where L_0 and L_1 are the membrane lengths and W_0 and W_1 are the membrane weights without and with water sorption, respectively [40].

2.10. Contact angle measurement

To determine hydrophilicity, contact-angle measurements were carried out between membrane surface and water by using a Tantec, CAM – Micro model, composed of three parts: a background light, a stand where the sample is placed, a needle above this stand, and a camera [41]. The measurements were performed with a water drop of 1 μL at 25°C. Also from the values of the water contact angle, free energy of hydration (ΔG_{SA}) of the membranes with water (subscript A) was calculated with the aim of quantifying their relative hydrophilicities from the water surface tension (γ_A^{TOT} = 73 mJ m^{-2}) [Eq. (5)] [42,43]:

$$(1 + \cos\theta)\gamma_A^{TOT} = -\Delta G_{SA} \tag{5}$$

2.11. Permeability and separation experiments

Permeability and separation experiments were performed using the following dead-end schema (Fig. 3) composed of a cell unit connected to a nitrogen gas line where pressure was controlled by a manometer, which forced the solution through the membrane. Before proceeding to the filtration, membranes were compacted for 2 h and put under pressure of 6 bar by passing distilled water. The feed solution was stirred magnetically to avoid concentration gradients during the filtration process. Distilled water permeability was calculated by Eq. (6):

$$J = \frac{\Delta V}{A \times t \times P} \tag{6}$$

where ΔV is the volume of permeance (L), A is the effective area of the membrane (9.62 cm^2), ΔT is the permeation time, and P is the used pressure (6 bar).

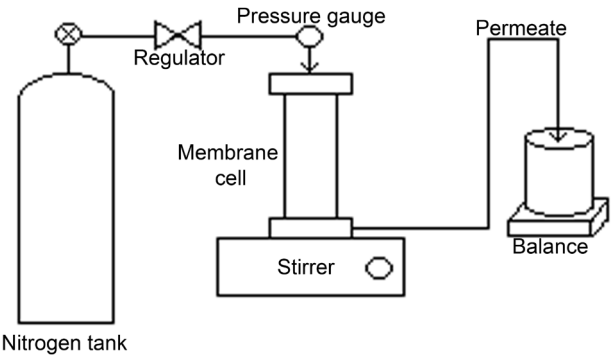

Fig. 3. Schematic illustration of the nanofiltration dead-end test cell.

To determine molecular weight cutoff, aqueous solutions of polyethylene glicol (PEG) (300; 400; 1,500; 4,000; and 6,000 g mol^{-1}) were used and the following salt solutions (NaCl, Na_2SO_4, $MgCl_2$, and $MgSO_4$) were used with a concentration of 1,000 mg L^{-1} to determine saline rejection. All reagents were supplied by Labsynth (Diadema, Brazil). Hence, rejection (R) was calculated by Eq. (7):

$$R = \left[1 - \frac{C_p}{C_f}\right] \times 100 \quad (7)$$

where C_p and C_f are the solute concentrations measured in permeate and feed, respectively.

3. Results and discussion

3.1. Silver nanoparticle characterization

The electronic spectrum of the diluted sample in deionized water (Fig. 4) revealed an absorption peak at 414 nm with a full width at half maximum attributed to the plasmonic band of the silver nanoparticles. This narrow width is a qualitative indication of the dispersivity of the size of the nanoparticles in solution, tending to monodispersion.

The nanoparticle size was determined by TEM from the dilutions of the sample. Fig. 5 allows observing spherical nanoparticles with homogeneous sizes, without aggregates. In the enlargement, a typical silver nanoparticle is shown. Moreover, from the analysis of the TEM images (Fig. 6), the average diameter was 3.34 nm.

3.2. Properties of the PSf/NMP/GRAFIM®/water and PSf/NMP/GRAFIM®+Ag/water systems

Concerning the PSf/NMP/GRAFIM® and PSf/NMP/GRAFIM®+Ag dispersions, a study which relates the shear stress with the shear rate for each of the dispersions is presented in Fig. 7 to clarify the effect of the GRAFIM® concentration and silver nanoparticle presence. For both systems, the shear stress was found to increase with the shear rate. Furthermore, as both of their linear regression is equal to 0.999, it can be concluded that the relations between shear stress and shear rate are linear and dispersions can be considered Newtonian fluids. The intercept of the linear regression can be neglected.

The influence of the GRAFIM® concentration and silver nanoparticle presence was also investigated in terms of intrinsic viscosity (η), as shown in Table 2. The addition of GRAFIM® increased viscosity for the 0.5 wt.% GRAFIM® dispersion due to the entanglements formed by the interactions established between the GRAFIM® and PSf chains. However, for the 1.0 and 2.0 wt.% GRAFIM®, viscosities were lower. This is due to the alignment of the larger entanglements formed by GRAFIM® particles and PSf chains in the shearing direction.

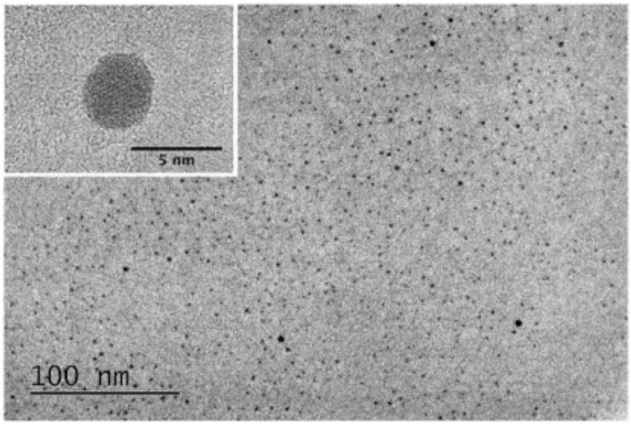

Fig. 5. Transmission electron microscopy of the silver nanoparticles. In the detail, the magnification of one of the nanoparticles.

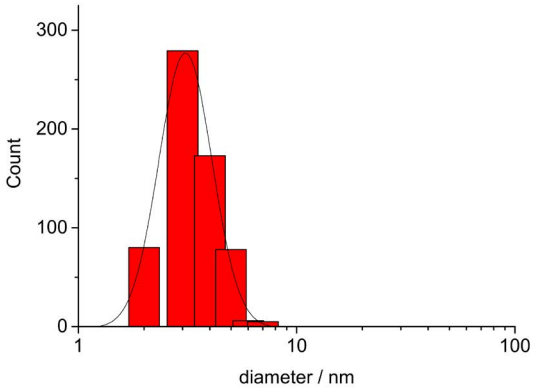

Fig. 6. Histogram of the size distribution obtained from the transmission electron microscopy of the sample.

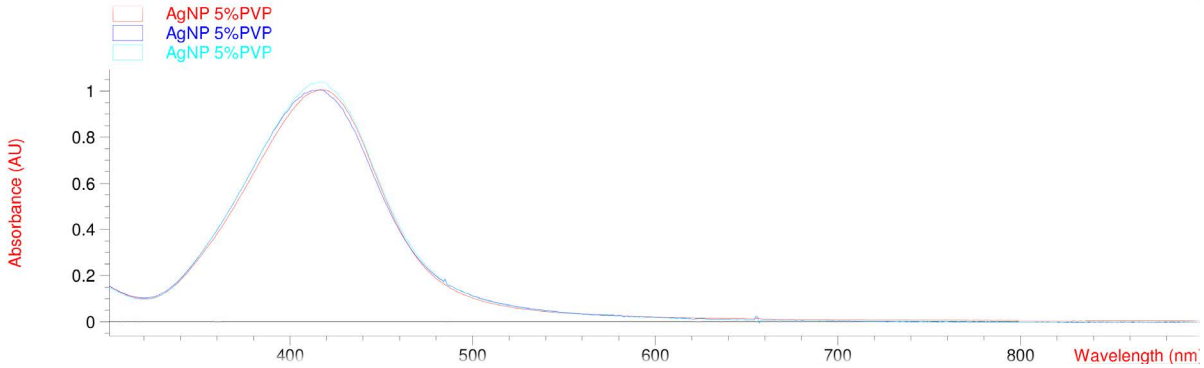

Fig. 4. UV-Vis spectrum of the silver nanoparticle solution.

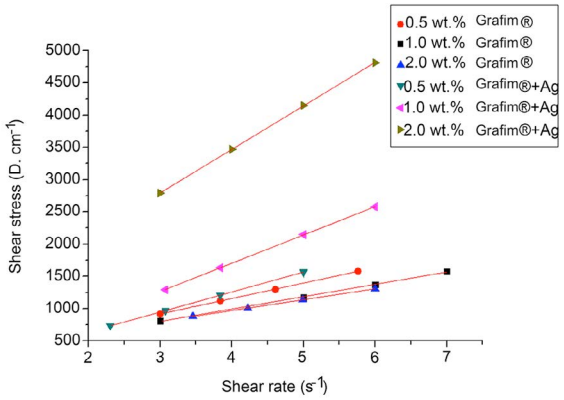

Fig. 7. Shear rate versus shear stress of PSf/NMP/GRAFIM® and PSf/NMP/GRAFIM®+Ag dispersions by varying the GRAFIM® content.

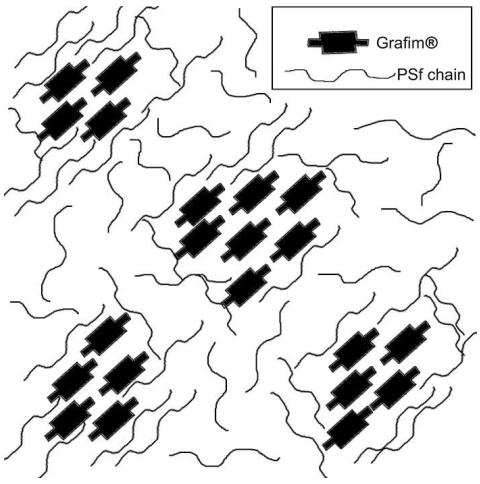

Fig. 8. Schematic representation of the entanglements formed by GRAFIM® particles and polysulfone chains.

Table 2
Linear regression equation and respective linear correlation coefficient (R^2) of each dispersion produced with GRAFIM® and GRAFIM® plus silver nanoparticles and their intrinsic viscosities (η)

Dispersion	Linear regression equation	R^2	η (cP)
0% GRAFIM®	$y = 93.18x + 65.82$	0.9999	7,071 [39]
0.5% GRAFIM®	$y = 239.02x + 201.99$	0.9990	37,729
1.0% GRAFIM®	$y = 191.07x + 231.14$	0.9997	30,998
2.0% GRAFIM®	$y = 168.43x + 298.4$	0.9996	30,580
0.5% GRAFIM®+Ag	$y = 309.48x + 20.637$	0.9999	43,924
1.0% GRAFIM®+Ag	$y = 438.11x - 48.091$	0.9999	47,743
2.0% GRAFIM®+Ag	$y = 674x + 772$	0.9999	54,583

Furthermore, as the silver nanoparticle dispersions had been stabilized with PVP and alcohol, they presented higher viscosities. Intra- and intermolecular interactions between PVP, silver nanoparticles, alcohol, and PSf chains are believed to have been established, forming greater entanglements than those formed only with GRAFIM® (Fig. 8). Hence, by increasing the GRAFIM® content in the presence of silver nanoparticles, intrinsic viscosity is augmented.

Understanding the kinetics of the systems is very important to explain membrane morphology. The kinetics of membrane formation is sharply influenced by the composition of the casting dispersion and the conditions of membrane preparation. As the dispersions in this experiment were turbid and dark, the kinetic study of the systems by optical microscopy [44] could not be carried out. Therefore, for each dispersion, membranes were prepared in different thicknesses by using an adjustable casting knife and the coagulation time of each membrane was related to its wet membrane thickness at 60°C.

The relationship between the square of the wet membrane thickness and the coagulation time of each dispersion is presented in Fig. 9. In all the equations, d^2 (cm^2) and t (s) are the square of the wet membrane thickness and the coagulation time, respectively. For all the dispersions, the square of the wet membrane thickness is linearly proportional to the coagulation time as their linear regression coefficients are larger than 0.997. The intercept is very small when compared with the minimum coagulation time, which corresponds to less than 1% of the lowest value of d^2. Thus, this intercept can be rejected. Therefore, this linear proportion demonstrated that the kinetic parameter of membrane formation D (cm s^{-2}) of both systems can be determined by the Second Fickian diffusion law [45]; this diffusion can be considered "Fickian." Water diffusion coefficients were obtained by Eq. (8) and are presented in Table 3:

$$d^2 = D \times t \quad \text{or} \quad D = \frac{d^2}{t} \tag{8}$$

Except for the 2.0 wt.% GRAFIM®+Ag dispersion, the water diffusion coefficients in the dispersions are in the same range presented in other systems (between 10^{-5} and 10^{-6} cm^2 s^{-1}) [10]. Furthermore, the increase in dispersion viscosity clearly had a negative impact on D. A decrease of the exchange rate was observed between solvent and nonsolvent. Consequently, PSf chains precipitate slowly, delaying the demixing process due to a rheological hindrance.

3.3. Morphological aspects of the composite membranes

The membrane surfaces can be seen in the SEM images (Fig. 10). The ones prepared with GRAFIM® formed dense surfaces. These formations are due to the hygroscopic character of NMP. Moreover, the PSf chains needed a smaller amount of water to precipitate because these macromolecules were adsorbed onto the GRAFIM® structure making them interact less with the solvent molecules. Therefore, a dense surface is a result of the fast exchange between solvent and nonsolvent, inducing a fast polymer collapse on the film surface [46]. On the other hand, in the membranes with silver nanoparticles, as dispersion viscosities are higher, the diffusion was delayed and nanopores could be observed.

The cross-sectional morphology revealed (SEM images, Fig. 11) that the liquid-liquid separation was so fast that

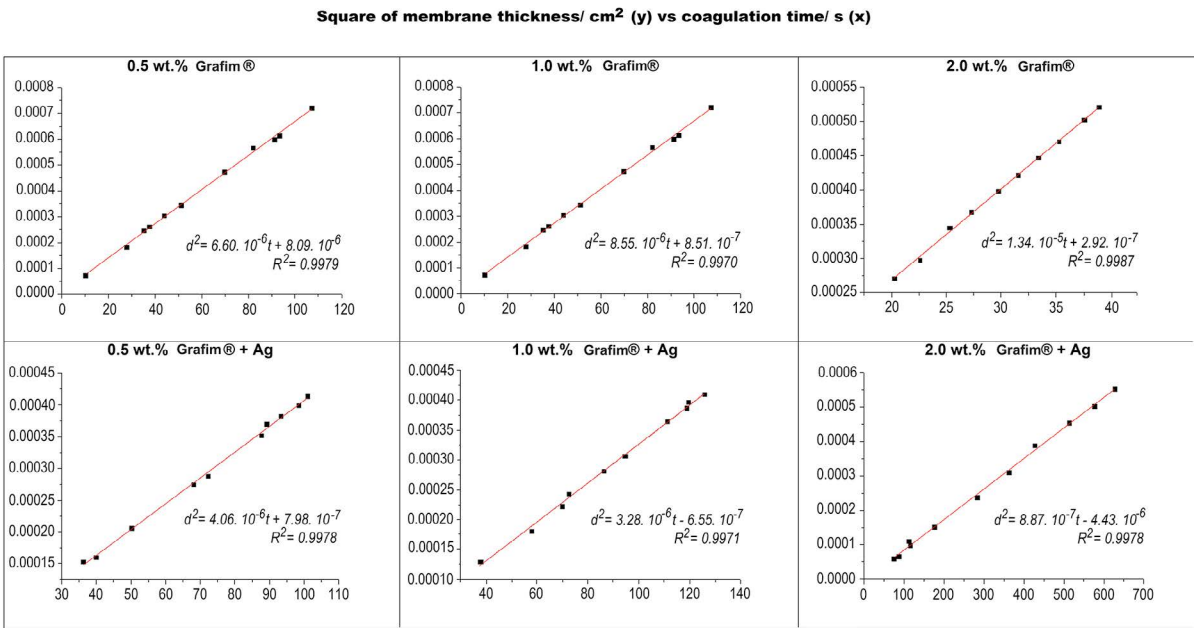

Fig. 9. The relationship between the square of the wet membrane thickness and the coagulation time of the PSf/NMP/GRAFIM®/water and PSf/NMP/GRAFIM®+Ag/water systems with different GRAFIM® contents.

Table 3
Water diffusion coefficients (D) of each dispersion produced with GRAFIM® and GRAFIM® plus silver nanoparticles

Dispersion	D (cm^2 s^{-1})
0% GRAFIM®	1.95×10^{-5} [39]
0.5% GRAFIM®	6.60×10^{-6}
1.0% GRAFIM®	8.55×10^{-6}
2.0% GRAFIM®	1.34×10^{-5}
0.5% GRAFIM®+Ag	4.06×10^{-6}
1.0% GRAFIM®+Ag	3.28×10^{-6}
2.0% GRAFIM®+Ag	8.87×10^{-7}

the GRAFIM® particles were prevented from leaching and became trapped in the membranes' pores (indicated by arrows). Because 0.5 wt.% GRAFIM® and all silver nanoparticle dispersions present the highest viscosities, a barrier was formed to nonsolvent diffusion as more water molecules entered the film. The reduction in diffusion caused the formation of finger-like macrovoids with irregular and more rounded shape. In contrast, by decreasing the viscosity, elongated finger-like macrovoids were formed as verified in the 1.0 and 2.0 wt.% GRAFIM® micrographs.

Specifically, membranes with silver nanoparticles were stabilized with PVP, which is a nonsolvent additive; this is known to have a contradictory effect: it reduces the stability of the casting dispersion, accelerating the phase separation process, but it also increases dispersion viscosity, delaying the liquid-liquid phase separation. This dual behavior derives from its chemical nature and its interaction with the polymer dispersion and nonsolvent [47].

Additionally, it is an opportunity to discuss the influence of viscosity on the macrovoid wall and membrane skin. In all membranes, a dense layer is followed by macrovoids with small pores in their interior. Since dispersion viscosities are far higher than the PSf solution viscosity [44], the conditions of coagulation of the nucleus wall and of the film-bath interface are different because diffusion is lower in the inner film.

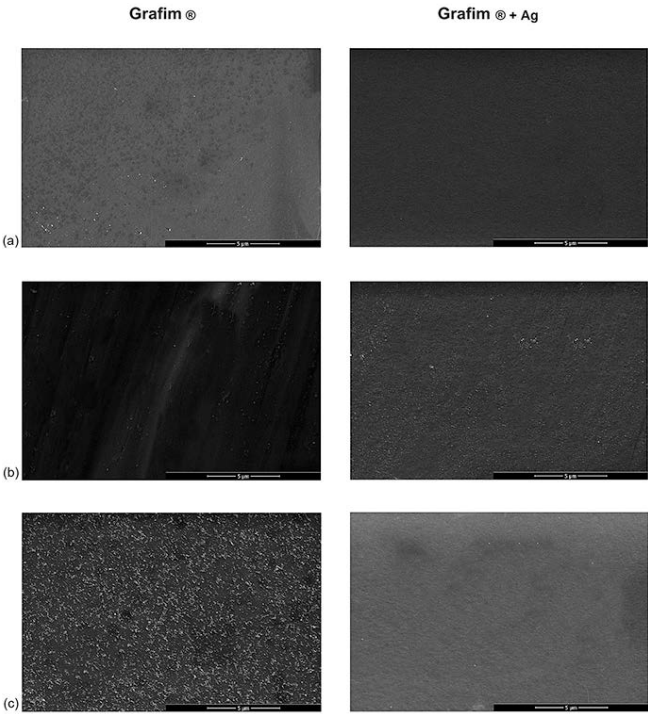

Fig. 10. SEM images of the PSf composite membrane surfaces according to the presence of silver nanoparticles and GRAFIM® content: (a) 0.5 wt.%, (b) 1.0 wt.%, and (c) 2.0 wt.%.

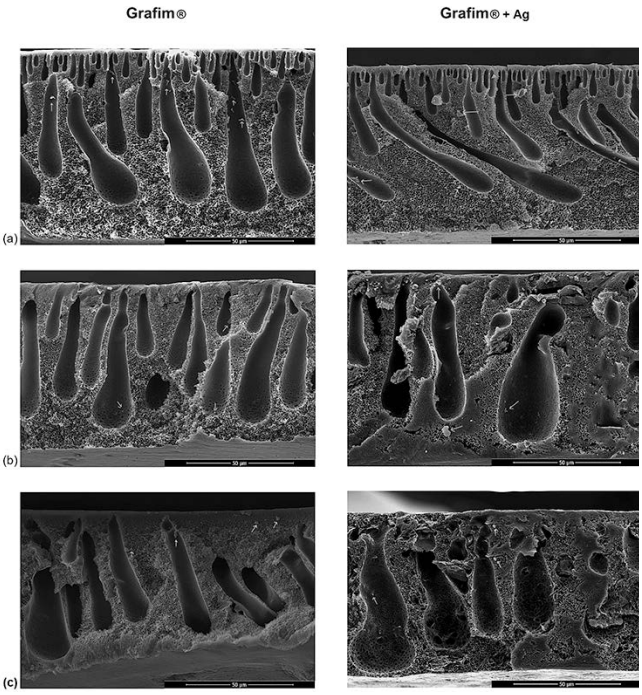

Fig. 11. SEM images of the PSf composite membrane cross sections according to the presence of silver nanoparticles and GRAFIM® content: (a) 0.5 wt.%, (b) 1.0 wt.%, and (c) 2.0 wt.%.

In other words, a fast collapse of the surface happened as a consequence of the addition of nonsolvent but, as the nonsolvent molecules moved onto the inner film, concentration gradients were formed due to the presence of GRAFIM® and silver nanoparticles, thus decreasing diffusion and forming pores on the macrovoid walls. A similar effect was observed for PSf-Aerosil membranes [10].

Thus, a complex interrelationship between thermodynamical favoring and rheological hindrance influences the liquid-liquid phase separation on the PSf/NMP/GRAFIM®/water and PSf/NMP/GRAFIM®+Ag/water systems. In other words, the presence of GRAFIM® and silver nanoparticles increases the thermodynamical instability, favoring diffusion; however, the higher viscosities deactivate mutual diffusivities between system components. As the diffusion-induced coagulation process begins to precipitate the dispersion, some thermodynamical driving forces are sacrificed due to the increase of system viscosity [48,49].

Membrane structures were also studied by atomic force microscopy (Fig. 12). The angle of view was 45°, aiming that the tridimensional characteristics of the images of the atomic microscopy are emphasized and all figures have scale *x-y* 8–8 μm. From the images, both the increase of GRAFIM® content and the addition of silver nanoparticles increased the rugosity of the membrane surface, presenting a ridge and valley structure. The membranes with lower GRAFIM® contents presented a smoother surface probably because intermolecular interactions were established between the PSf chains and the GRAFIM® particles. When the additive content is exceeded, agglomerations are formed, and the surface becomes more rugous. The bright areas in the images represent the additives used in the membrane preparation [50].

3.4. Composite membrane properties

Table 4 summarizes the porosities of the membranes produced with GRAFIM® and GRAFIM® plus silver nanoparticles. Their values are in the range of 73.1%–88.9%, which shows that the addition of GRAFIM® and especially of silver nanoparticles had a positive impact on the overall porosity of composite membranes, and these high values can be explained by the abundance of finger-like macrovoids detected in the cross-sectional morphology. The magnitude of these values is also due to the increase of viscosity, which hampered the exchange between solvent and nonsolvent, delaying liquid-liquid phase separation. Hence, the membranes produced with dispersions with higher viscosities had higher porosities. In addition, the higher values of porosities of the silver nanoparticle membranes are also due to the presence of PVP, which is known to act as pore former [47].

Also, in Table 4, the water sorption and linear expansion of each membrane are presented. Although hydrophilicity and porosity are known to influence this feature, membrane porosity was mainly responsible for the increase of the water sorption in these membranes, once again related to higher dispersion viscosities. That is, GRAFIM® and silver nanoparticles only helped the membrane wettability, but porosity was paramount to define water sorption.

In contrast, the linear expansion only depends on the membrane structure, and for this reason, no significant differences were observed for linear expansion values by varying the GRAFIM® content and the presence of silver nanoparticles. These values are only higher than the pure PSf membrane, which could mean that, as the water sorption of the composite membranes is considerable, the composite membranes tend to expand more than the pure PSf membrane thus having higher values. Even so, if we consider that the water sorption of the composite membranes is extremely high in comparison with the pure PSf membrane, these linear expansion values are understood to be extremely low. That is because of the dimensional stability conferred by the composite formation and consequent chemical interaction between the PSf chains and the additive. Also, the GRAFIM® particles act as a barrier to water diffusion. Additionally, these membranes have bulbous macrovoids; these larger pores can hold more water, contributing to better stability.

Comparing with the pure PSf membrane, it is possible to conclude that both GRAFIM® addition and the presence of silver nanoparticles produced membranes with a highly hydrophilic character, since the real hydrophilic materials have ΔG_{S_A} equal to or lower than −113 mJ m^{-2} [51]. Also, an increase of the contact angle with the presence of silver nanoparticles was observed with the increase of the GRAFIM® content, which can be explained by the higher rugosity of the membrane surfaces, because hydrophilicity is dependent on the chemical groups of the membrane surface and porosity and rugosity [52]. In this case, the effect of increasing rugosity was crucial to a slight decrease of the membrane hydrophilicity. If membranes were smooth and silver nanoparticles were added, we would observe a gradual increase on hydrophilicity by augmenting GRAFIM® content. As there is not a great difference in membrane porosity, the final hydrophilicity would not be affected.

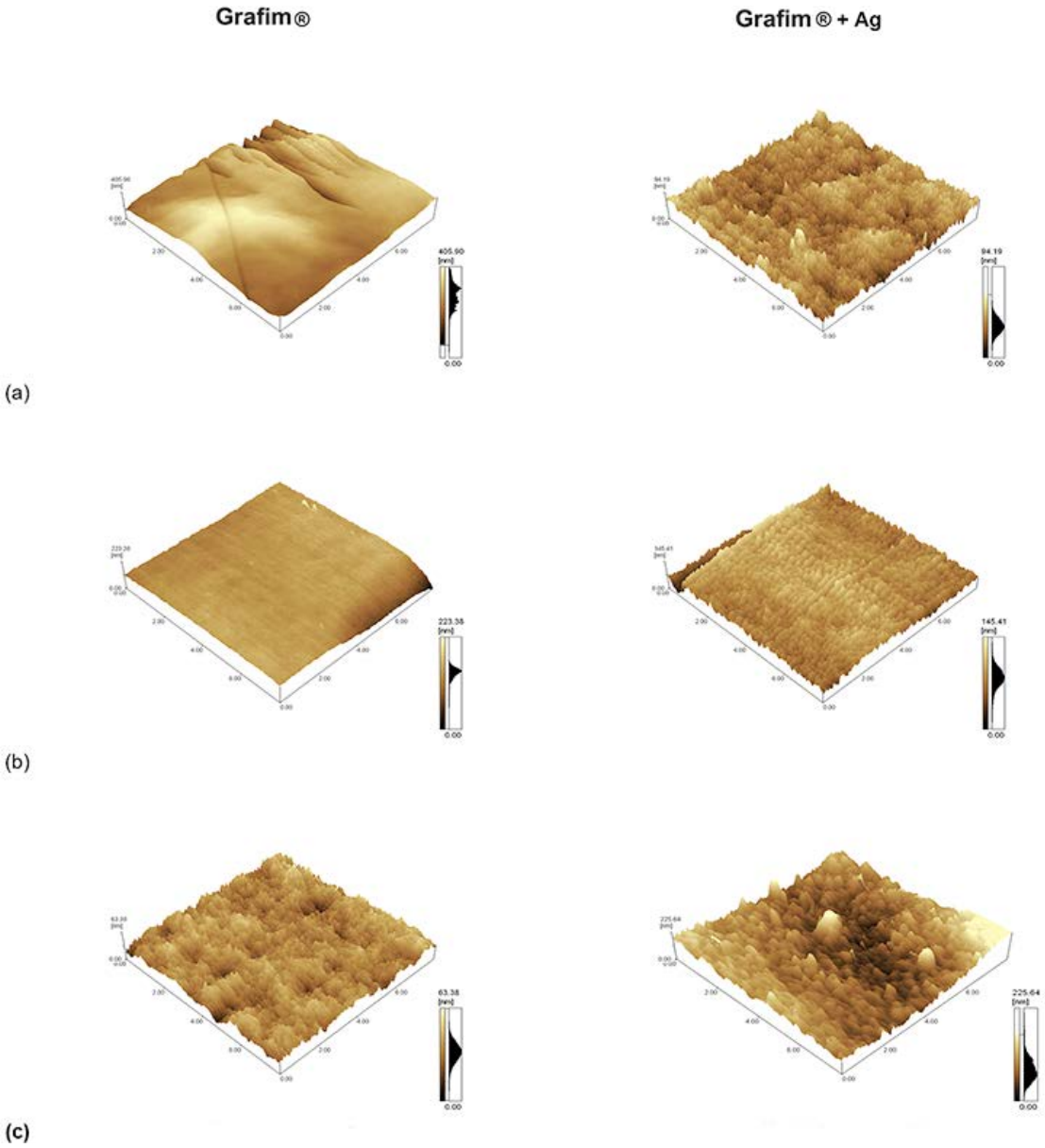

Fig. 12. AFM images of the PSf composite membrane cross sections according to the presence of silver nanoparticles and GRAFIM® content: (a) 0.5 wt.%, (b) 1.0 wt.%, and (c) 2.0 wt.%.

Table 4
Porosity (*P*), linear expansion (*L*), and water sorption (*W*) of the membranes produced with Recam® and Recam® plus silver nanoparticles

Dispersion	*P* (%)	*W* (%)	*L* (%)
0% GRAFIM®	51.3 ± 4.1	13.6 ± 0.9	1.19 ± 0.06 [44]
0.5% GRAFIM®	75.9 ± 2.1	163.1 ± 2.7	2.33 ± 0.02
1.0% GRAFIM®	73.5 ± 3.2	159.4 ± 1.4	2.11 ± 0.03
2.0% GRAFIM®	73.1 ± 1.7	148.2 ± 2.4	2.03 ± 0.06
0.5% GRAFIM®+Ag	84.9 ± 2.2	170.7 ± 3.2	2.07 ± 0.02
1.0% GRAFIM®+Ag	85.8 ± 1.2	175.2 ± 2.7	2.23 ± 0.04
2.0% GRAFIM®+Ag	88.9 ± 3.9	179.1 ± 1.8	2.35 ± 0.01

3.5. Filtration performance

Table 5 shows the distilled water permeability. Permeation values between 1.9× and 1.65× higher than pure PSf membranes were obtained. In the case of the membranes with only GRAFIM®, the highest value of water flux was observed for the membrane with 0.5 wt.% GRAFIM®, whereas the membranes with silver nanoparticles, 2.0 wt.% GRAFIM®, produced the highest value of all. The permeability results revealed their dependence on two factors: the higher the porosity and hydrophilicity, the higher the water permeability. The presence of silver nanoparticles and GRAFIM® increased hydrophilicity and also promoted a connection between pores, facilitating the passage of water molecules. However, according to the obtained results, the

Table 5
Water permeability and its used pressure (in superscript, bar unit) and salt retention of the membranes produced with GRAFIM® and GRAFIM® plus silver nanoparticles and commercial membranes

Membrane	Water permeability ($L\ m^{-2}\ h^{-1}\ bar^{-1}$)	Na_2SO_4 (%)	NaCl (%)	$MgSO_4$ (%)	$MgCl_2$ (%)
0% GRAFIM®	$^{4.6}37.8$ [44]	–	5.1	–	–
0.5% GRAFIM®	$^{6.0}63.5$	90.9	89.4	67.4	39.1
1.0% GRAFIM®	$^{6.0}62.9$	92.7	90.8	72.1	42.0
2.0% GRAFIM®	$^{6.0}62.7$	96.4	95.2	73.8	44.1
0.5% GRAFIM®+Ag	$^{6.0}69.7$	85.9	83.9	56.5	35.9
1.0% GRAFIM®+Ag	$^{6.0}70.1$	87.6	88.0	57.0	38.5
2.0% GRAFIM®+Ag	$^{6.0}72.3$	90.5	87.7	57.7	39.7
NTR-7410 [56]	$^{10}49.6$	55	15	9	4
NTR-7450 [56]	$^{10}9.4$	92	51	32	13

permeation across the membrane was more dependent on porosity.

Fig. 13 presents the rejection values to PEG with different molecular weights. The rejection values were higher for the membranes without silver nanoparticles as the fast exchange between solvent and nonsolvent produced dense surfaces which retain lower molecular weight PEG. Moreover, GRAFIM® is known as a great filter; hence, PEG retention was also helped by GRAFIM® presence. In these membranes, rejection was reduced by increasing GRAFIM® content since macrovoids are bigger. Even so, the cutoffs are between 300 and 400 g mol^{-1} for the membranes with 0.5 and 1.0 wt.% GRAFIM® and slightly higher than 400 g mol^{-1} for the membrane with 2.0 wt.% GRAFIM®. Since the membranes with silver nanoparticles presented nanopores on their surfaces due to the induction of PVP, their cutoffs were higher, between 400 and 1,500 g mol^{-1}. PEG rejection was also lower due to the presence of elongated macrovoids, which were bigger on the membranes with higher GRAFIM® contents. Therefore, both types of membranes can be considered as nanofiltration membranes as their cutoffs are in the range of 200–2,000 Da.

For the saline rejection, two effects were responsible for the ion retention: size exclusion and Donnan effect (Fig. 14). The first one is observed especially comparing membranes with and without silver nanoparticles. As the surfaces of the last membranes are dense, their rejection values were higher in relation to the membranes with silver nanoparticles. Moreover, the Donnan effect plays an important role in the saline rejection. The π electrons of the graphene are responsible for the overall negative charge of the membrane that attracts the cations causing rejection by electronic effects. In order to maintain the charge neutrality on the feed side, the anions are also rejected by the Donnan effect. Increasing GRAFIM® content in both types of membranes caused increased saline rejection. Rejection took place in both membranes according to the sequence presented in Fig. 14: Na_2SO_4 > NaCl > $MgSO_4$ > $MgCl_2$. The ionic radii of hydrated ions are reported as follows: Na^+, 0.358 nm; Mg^{2+}, 0.428 nm; Cl^-, 0.332 nm; and SO_4^{2-}, 0.379 nm [53]. If the filtration was governed by size exclusion, $MgSO_4$ would

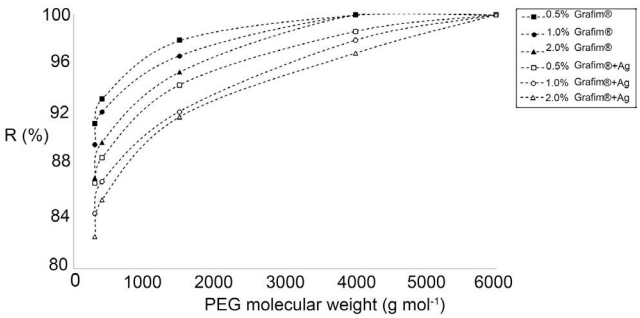

Fig. 13. PEG rejections of the membranes with GRAFIM® and silver nanoparticles.

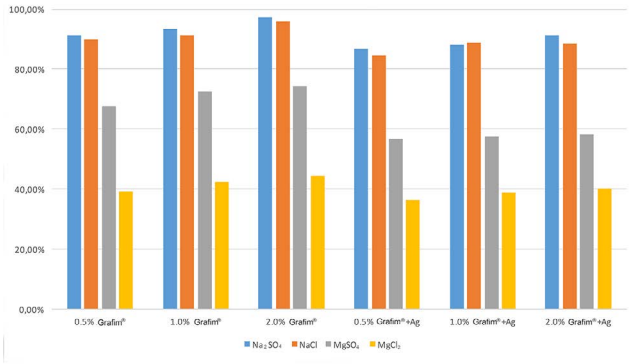

Fig. 14. Saline rejections (NaCl, Na_2SO_4, $MgCl_2$, and $MgSO_4$) of the membranes with GRAFIM® and silver nanoparticles.

have the highest retention as its ions are bigger. However, as these membranes are negatively charged, both sodium ions (monovalent ions) and counter-ions are attracted to membrane surface. Nevertheless, sulfate ions (bivalent ions) are repulsed, presenting the highest rejection. Conversely, the magnesium ion, which is a bivalent ion, is less attracted

to membrane surface, and chloride ions, monovalent ions, are less rejected than sulfate ions, thus presenting the lowest rejection. This result is in agreement with the negatively charged membranes, in which the Donnan effect is responsible for the exclusion [54,55].

To compare composite membrane performance with commercial membranes, water permeabilities and salt rejections of the developed membranes and some commercial membranes are also presented in Table 5. The chosen commercial membranes are, respectively, NTR-7410 and NTR-7450 by Nitto-Denko (Osaka, Japan) Membranes [56]. The developed membranes present better salt rejections, as well as higher water permeabilities under lower pressures, useful to water filtration.

4. Conclusions

We studied the influence of viscosity on PSf/GRAFIM® and PSf/GRAFIM®/silver nanoparticle membrane properties. The following conclusions can be drawn:

- The 1.0 and 2.0 wt.% GRAFIM® dispersions present lower intrinsic viscosities than 0.5 wt.% because their entanglements are aligned in the direction of shearing. Increasing GRAFIM® content augments silver nanoparticle dispersion viscosity.
- Diffusion coefficients of all dispersions followed the Second Fickian law. The increase of dispersion viscosity decreased the diffusion coefficient.
- The GRAFIM® membrane surface is dense due to the hygroscopic character of NMP and to the adsorption of the PSf chain onto the GRAFIM® structure. Conversely, silver nanoparticle membranes have nanopores on their surfaces, presenting high viscosity which delays diffusion. The higher viscosities of the 0.5 wt.% GRAFIM® and silver nanoparticle dispersions are responsible for the irregular and rounded macrovoids in the cross-sectional morphology because a barrier is formed to nonsolvent diffusion. In conclusion, two factors guide the liquid-liquid phase separation on the two systems: thermodynamical favoring and rheological hindrance. Furthermore, both additives contributed to the increase of rugosity on the membrane surface.
- The addition of GRAFIM® and GRAFIM® plus silver nanoparticles provides the formation of a high level of porosity due to the delay of the liquid-liquid phase separation. Moreover, the membranes with silver nanoparticles present the highest porosities since PVP acts as a pore former.
- Water sorption also depends on dispersion viscosity as the higher the membrane porosity, the higher the water sorption. On the other hand, there are no significant differences for linear expansion values by varying the GRAFIM® content and the presence of silver nanoparticles. Real hydrophilic materials were produced by using GRAFIM® and silver nanoparticles.
- High values of water permeability were obtained due to the high membrane porosity and the hydrophilicity. These values were higher for the membranes with silver nanoparticles due to the presence of nanopores. All membrane cutoffs were in the range of nanofiltration. Saline rejection showed its dependence on size exclusion and primordially on Donnan effect.

Acknowledgements

The authors would like to thank Prof. Henrique Kahn, PhD, and Renato Contessotto, MSc, for helping us with the SEM images, and Solvay is also acknowledged for providing PSf Udel® P-1700 and Udel® P-3500. Also, Sergio H. Toma, PhD, and Prof. Henrique E. Toma, PhD, are acknowledged for helping us with the silver nanoparticles. We would also like to thank Ivano Aglietto, PhD, from GrapheneUP SE, for providing us GRAFIM®. Finally, this study was financed in part by the Coordenação de Aperfeiçoamento de Pessoal de Nível Superior – Brazil (CAPES) – Finance Code 001.

References

[1] S. Mokhtari, A. Rahimpour, A.A. Shamsabadi, S. Habibzadeh, M. Soroush, Enhancing performance and surface antifouling properties of polysulfone ultrafiltration membranes with salicylate-alumoxane nanoparticles, Appl. Surf. Sci., 393 (2017) 93–102.
[2] C. Xu, X. Liu, B. Xie, C. Yao, W. Hu. Y. Li, X. Li, Preparation of PES ultrafiltration membranes with natural amino acids based zwitterionic antifouling surfaces, Appl. Surf. Sci., 385 (2016) 130–138.
[3] Q. Nan, P. Li, B. Cao, Fabrication of positively charged nanofiltration membrane via the layer-by-layer assembly of graphene oxide and polyethylenimine for desalination, Appl. Surf. Sci., 387 (2016) 521–528.
[4] M. Yang, C. Zhao, S. Zhang, P. Li, D. Hou, Preparation of graphene oxide modified poly(m-phenylene isophthalamide) nanofiltration membrane with improved water flux and antifouling property, Appl. Surf. Sci., 394 (2017) 149–159.
[5] S. Shanmuganathan, P. Loganathan, C. Kazner, M.A.H. Johir, S. Vigneswaran, Submerged membrane filtration adsorption hybrid system for the removal of organic micropollutants from a water reclamation plant reverse osmosis concentrate, Desalination, 401 (2017) 134–141.
[6] D. Zhao, Y. Yu, C. Wang, J.P. Chen, Zirconium/PVA modified flat-sheet PVDF membrane as a cost-effective adsorptive and filtration material: a case study on decontamination of organic arsenic in aqueous solutions, J. Colloid Interface Sci., 477 (2016) 191–200.
[7] H. Guo, J. Wang, Y. Han, Y. Feng, K. Shih, C.Y. Tang, Removal of perfluorooctane sulfonate by a gravity-driven membrane: filtration performance and regeneration behavior, Sep. Purif. Technol., 174 (2017) 136–144.
[8] E. Shokri, R. Yegani, B. Pourabbas, N. Kazemian, Preparation and characterization of polysulfone/organoclay adsorptive nanocomposite membrane for arsenic removal from contaminated water, Appl. Clay Sci., 132 (2016) 611–620.
[9] P. Anadão, R.R. Montes, N.M. Larocca, L.A. Pessan, Influence of the clay content and the polysulfone molar mass on nanocomposite membrane properties, Appl. Surf. Sci., 275 (2013) 110–120.
[10] P. Aerts, E. Van Hoof, R. Leysen, I.F.J. Vankelecom, P.A. Jacobs, Polysulfone–Aerosil composite membranes: Part 1. The influence of the addition of Aerosil on the formation process and membrane morphology, J. Membr. Sci., 176 (2000) 63–73.
[11] X. Zhao, Y. Su, Y. Liu, R. Zhang, Z. Jiang, Multiple antifouling capacities of hybrid membranes derived from multifunctional titania nanoparticles, J. Membr. Sci., 495 (2015) 226–234.
[12] Q. Wang, G.-S. Zhang, Z.-S. Li, S. Deng, H. Chen, P. Wang, Preparation and properties of polyamide/titania composite nanofiltration membrane by interfacial polymerization, Desalination, 352 (2014) 38–44.

[13] A. Razmjou, J. Mansouri, V. Chen, M. Lim, R. Amal, Titania nanocomposite polyethersulfone ultrafiltration membranes fabricated using a low temperature hydrothermal coating process, J. Membr. Sci., 380 (2011) 98–113.
[14] M.T.M. Pendergast, A.K. Ghosh, E.M.V. Hoek, Separation performance and interfacial properties of nanocomposite reverse osmosis membranes, Desalination, 308 (2013) 180–185.
[15] E.M.V. Hoek, A.K. Ghosh, X. Huang, M. Liong, J.I. Zink, Physical–chemical properties, separation performance, and fouling resistance of mixed-matrix ultrafiltration membranes, Desalination, 283 (2011) 89–99.
[16] A.K. Zulhairun, A.F. Ismail, T. Matsuura, M.S. Abdullah, A. Mustafa, Asymmetric mixed matrix membrane incorporating organically modified clay particle for gas separation, Chem. Eng. J., 241 (2014) 495–503.
[17] Y. Ma, F. Shi, W. Zhao, M. Wu, J. Zhang, J. Ma, C. Gao, Preparation and characterization of PSf/clay nanocomposite membranes with LiCl as a pore forming additive, Desalination, 303 (2012) 39–47.
[18] Y. Ma, F. Shi, Z. Wang, M. Wu, J. Ma, C. Gao, Preparation and characterization of PSf/clay nanocomposite membranes with PEG 400 as a pore forming additive, Desalination, 286 (2012) 131–137.
[19] K. Zarshenas, A. Raisi, A. Aroujalian, Mixed matrix membrane of nano-zeolite NaX/poly (ether-block-amide) for gas separation applications, J. Membr. Sci., 510 (2016) 270–283.
[20] N.A. Ahmad, C.P. Leo, M.U.M. Junaidi, A.L. Ahmad, PVDF/PBI membrane incorporated with SAPO-34 zeolite for membrane gas absorption, J. Taiwan Inst. Chem. Eng., 63 (2016) 143–150.
[21] Y. Yurekli, Removal of heavy metals in wastewater by using zeolite nano-particles impregnated polysulfone membranes, J Hazard. Mater., 309 (2016) 53–64.
[22] M.-B. Wu, Y. Lv, H.-C. Yang, L.-F. Liu, X. Zhang, Thin film composite membranes combining carbon nanotube intermediate layer and microfiltration support for high nanofiltration performances, J. Membr. Sci., 515 (2016) 238–244.
[23] H. Zarrabi, M.E. Yekavalangi, V. Vatanpour, A. Shockravi, M. Safarpour, Improvement in desalination performance of thin film nanocomposite nanofiltration membrane using amine-functionalized multiwalled carbon nanotube, Desalination, 394 (2016) 83–90.
[24] Y.C. Woo, Y. Kim, W.-G. Shim, L.D. Tijing, M. Yao, L.D. Nghiem, J.-S. Choi, S.-H. Kim, H.K. Shon, Graphene/PVDF flat-sheet membrane for the treatment of RO brine from coal seam gas produced water by air gap membrane distillation, J. Membr. Sci., 513 (2016) 74–84.
[25] S. Qiu, L. Wu, X. Pan, L. Zhang, H. Chen, C. Gao, Preparation and properties of functionalized carbon nanotube/PSF blend ultrafiltration membranes, J. Membr. Sci., 342 (2009) 162–172.
[26] E. Celik, H. Park, H. Choi, H. Choi, Carbon nanotube blended polyethersulfone membranes for fouling control in water treatment, Water Res., 45 (2011) 274–282.
[27] J.-H. Choi, J. Jegal, W.-N. Kim, Fabrication and characterization of multi- walled carbon nanotubes/polymer blend membranes, J. Membr. Sci., 284 (2006) 406–415.
[28] H. Wu, B. Tang, P. Wu, Novel ultrafiltration membranes prepared from a multi- walled carbon nanotubes/polymer composite, J. Membr. Sci., 362 (2010) 374–383.
[29] P. Anadão, L.F. Sato, H. Wiebeck, F.R. Valenzuela-Díaz, Polysulfone activated carbon composite membranes, Mater. Sci. Forum, 660 (2010) 1081–1086.
[30] N. Ghaemi, S.S. Madaeni, A. Alizadeh, H. Rajabi, P. Daraei, Preparation, characterization and performance of polyethersulfone/organically modified montmorillonite nanocomposite membranes in removal of pesticides, J. Membr. Sci., 382 (2011) 135–147.
[31] C. Dong, Z. Wang, J. Wu, Y. Wang, J. Wang, S. Wang, A green strategy to immobilize silver nanoparticles onto reverse osmosis membrane for enhanced anti-biofouling property, Desalination, 401 (2017) 32–41.
[32] S.-H. Park, S.H. Kim, S.-J. Park, S. Ryoo, K. Woo, J.S. Lee, T.-S. Kim, H.-D. Park, H. Park, Y.-I. Park, J. Cho, J.-H. Lee, Direct incorporation of silver nanoparticles onto thin-film composite membranes via arc plasma deposition for enhanced antibacterial and permeation performance, J. Membr. Sci., 513 (2016) 226–235.
[33] E. Yang, K.-J. Chae, A.B. Alayande, K.-Y. Kim, I.S. Kim, Concurrent performance improvement and biofouling mitigation in osmotic microbial fuel cells using a silver nanoparticle-polydopamine coated forward osmosis membrane, J. Membr. Sci., 513 (2016) 217–225.
[34] Y. Feng, G. Han, L. Zhang, S.-B. Chen, T.-S. Chung, M. Weber, C. Staudt, C. Maletzko, Rheology and phase inversion behavior of polyphenylenesulfone (PPSU) and sulfonated PPSU for membrane formation, Polymer, 99 (2016) 72–82.
[35] A.F. Ismail, P.Y. Lai, Effects of phase inversion and rheological factors on formation of defect-free and ultrathin-skinned asymmetric polysulfone membranes for gas separation, Sep. Purif. Technol., 33 (2003) 127–143.
[36] P. Anadão, R.R. Montes, H.S. de Santis, H. Wiebeck, Rheology assessment of PSf/ NMP solution and its influence on membrane structure, Defect Diffus. Forum, 326–328 (2012) 422–427.
[37] L.C. Courrol, F.R.O. Silva, L. Gomes, A simple method to synthesize silver nanoparticles by photo-reduction, Colloids Surf. A Physicochem. Eng. Asp., 305 (2007) 54–57.
[38] S. Heilman, Efeito da radiação ionizante nos revestimentos de cateteres de poliuretano com nanopartículas de prate, Ph.D. Thesis, University of São Paulo, São Paulo, 2015.
[39] Q.-Z. Zheng, P. Wang, Y.-N. Yang, D.-J. Cui, The relationship between porosity and kinetics parameter of membrane formation in PSF ultrafiltration membrane, J. Membr. Sci., 286 (2006) 7–11.
[40] S.-L. Chen, A.B. Bocarsly, J. Benziger, Nafion-layered sulfonated polysulfone fuel cell membranes, J. Power Sources, 152 (2005) 27–33.
[41] T. Zhao, L. Jiang. Contact angle measurement of natural materials, Colloids Surf. B Biointerfaces, 161 (2018) 324–330.
[42] J.-F. Lapointe, S.F. Gauthier, Y. Pouliot, C. Bouchard, Characterization of interactions between β-lactoglobulin tryptic peptides and a nanofiltration membrane: impact on the surface membrane properties as determined by contact angle measurements, J. Membr. Sci., 261 (2005) 36–48.
[43] R. Du, A. Chakma, X. Feng, Poly(N,N-dimethylaminoethyl methacrylate)/polysulfone composite membranes for gas separations, J. Membr. Sci., 279 (2006) 76–85.
[44] P. Anadão, L.F. Sato, R.R. Montes, H.S. De Santis, Polysulphone/ montmorillonite nanocomposite membranes: effect of clay addition and polysulphone molecular weight on the membrane properties, J. Membr. Sci., 455 (2014) 187–199.
[45] H. Strathmann, K. Kock, P. Amar, R.W. Baker, The formation mechanism of asymmetric membranes, Desalination, 16 (1975) 179–203.
[46] M.-J. Han, S.-T. Nam, Thermodynamic and rheological variation in polysulfone solution by PVP and its effect in the preparation of phase inversion membrane, J. Membr. Sci., 202 (2002) 55–61.
[47] L. Marbelia, M.R. Bilad, A. Piassecka, P.S. Jishna, P.V. Naik, I.F.J. Vankelecom, Study of PVDF asymmetric membranes in a high-throughput membrane bioreactor (HT-MBR): influence of phase inversion parameters and filtration performance, Sep. Purif. Technol., 162 (2016) 6–13.
[48] M.-J. Han, S.-T. Nam, Thermodynamic and rheological variation in polysulfone solution by PVP and its effect in the preparation of phase inversion membrane, J. Membr. Sci., 202 (2002) 55–61.
[49] Y.S. Hang, H.J. Kim, U.Y. Kim, Asymmetric membrane formation via immersion precipitation method. I. Kinetic effect, J. Membr. Sci., 60 (1991) 219–232.
[50] V. Vatanpour, M. Safarpour, A. Khatee, H. Zarrabi, M.E. Yekavalangia, M. Kaviana, A thin film nanocomposite reverse osmosis membrane containing amine-functionalized carbon nanotubes, Sep. Purif. Technol., 184 (2017) 135–143.
[51] C.J. van Oss, Interfacial Forces in Aqueous Media, Marcel Dekker, New York, 1994.
[52] G.J. Summers, M.P. Ndawuni, C.A. Summers, Dipyridyl functionalized polysulfones for membrane production, J. Membr. Sci., 226 (2003) 21–33.

[53] E.R. Nightingale Jr., Phenomenological theory of ion solvation. Effective radii ofhydrated ions, J. Phys. Chem., 63 (1959) 1381–1387.
[54] K. Takeuchi, Y. Takizawa, H. Kitazawa, M. Fujii, K. Hosaka, J. Ortiz-Medina, A. Morelos-Gomez, R. Cruz-Silva, M. Fujishige, N. Akuzawa, M. Endo, Salt rejection behavior of carbon nanotube-polyamide nanocomposite reverse osmosis membranes in several salt solutions, Desalination, 443 (2018) 165–171.
[55] J.M.M. Peeters, J.P. Boom, M.H.V. Mulder, H. Strathmann, Retention measurements of nanofiltration membranes with electrolyte solutions, J. Membr. Sci., 145 (1998) 199–209.
[56] K. Ikeda, T. Takano, H. Ito, T. Kubota, S. Yamamoto, New composite charged reverse osmosis membrane, Desalination, 68 (1988) 109–119.